1   **Estimation of subsurface porosities and thermal conductivities of polygonal tundra by**

2   **coupled inversion of electrical resistivity, temperature, and moisture content data**

4   Elchin E. Jafarov[1], Dylan R. Harp[1], Ethan T. Coon[2], Baptiste Dafflon[3], Anh Phuong Tran[3,4],

5   Adam L. Atchley[1], Youzuo Lin[1], and Cathy J. Wilson[1]

7   1. Earth and Environmental Sciences Division, Los Alamos National Laboratory, Los Alamos,

8   New Mexico, USA

9   2. Climate Change Science Institute and Environmental Sciences, Oak Ridge National

10   Laboratory, Oak Ridge, Tennessee, USA

11   3. Climate and Ecosystem Division, Lawrence Berkeley National Laboratory, Berkeley,

12   California, USA

13   4. Department of Water Research Engineering and Technology, Water Research Institute,

14   Hanoi, Vietnam

17   **Abstract**

18   Studies indicate greenhouse gas emissions following permafrost thaw will amplify current rates of

19   atmospheric warming, a process referred to as the permafrost carbon feedback. However, large

20   uncertainties exist regarding the timing and magnitude of the permafrost carbon feedback, in part

21   due to uncertainties associated with subsurface permafrost parameterization and structure.

22   Development of robust parameter estimation methods for permafrost-rich soils is becoming urgent

23   under accelerated warming of the Arctic. Improved parameterization of the subsurface properties

24   in land system models would lead to improved predictions and reduction of modeling uncertainty.

25   In this work we set the groundwork for future parameter estimation (PE) studies by developing

26   and evaluating a joint PE algorithm that estimates soil porosities and thermal conductivities from

27   time-series of soil temperature and moisture measurements, and discrete in-time electrical

28   resistivity measurements. The algorithm utilizes the Model Independent Parameter Estimation and

29   Uncertainty Analysis toolbox and coupled hydro-thermal-geophysical modeling. We test the PE

30   algorithm against synthetic data, providing a proof-of-concept for the approach. We use specified

31 subsurface porosities and thermal conductivities and coupled models to setup a synthetic state,
32 perturb the parameters, then verify that our PE method is able to recover the parameters and
33 synthetic state. To evaluate the accuracy and robustness of the approach we perform multiple tests
34 for a perturbed set of initial starting parameter combinations. In addition, we varied types and
35 quantities of data to better understand the optimal dataset needed to improve the PE method. The
36 results of the PE tests suggest that using multiple types of data improve the overall robustness of
37 the method. Our numerical experiments indicate that special care needs to be taken during data
38 collection and the experiment setup, so that vertical distance between adjacent temperature and
39 soil moisture measuring sensors allows the signal variability in space and longer time interval
40 between resistivity snapshots allows signal variability in time.

41

42

43 **1. Introduction**

44 Subsurface soil property parametrization contributes to a wide uncertainty range in projected
45 active layer depth and in simulated permafrost distribution in the Northern Hemisphere when
46 predicted using Land System Models (Koven et al., 2015; Harp et al., 2016). Reduction of this
47 uncertainty is becoming urgent with recent accelerated thawing of permafrost (Biskaborn et al.,
48 2019). Warming permafrost leads to increased infrastructure maintenance costs (Hjort et al., 2018),
49 has a positive feedback on global climate change (McGuire et al., 2018), and increases the
50 probability of the potential hazards for human health (Schuster et al., 2018). Better subsurface soil
51 property parametrizations in Land System Models requires the development of methods that can
52 robustly estimate these soil properties including porosity and thermal conductivity of peat and
53 mineral layers.

54 Direct measurements of subsurface soil properties are labor intensive, destructive, and not always
55 feasible (Smith and Tice, 1988; Kern, 1994; Boike and Roth, 1997; Yoshikawa et al., 2004). While
56 soil sample analysis can provide critical information on soil properties at a fine scale, this
57 information is limited to sparsely sampled locations. Multiple methods used in the laboratory to
58 measure soil properties by using soil cores extracted from the field site are well summarized by
59 Nicolsky et al., (2009), but logistical and economic burden typically do not allow these
60 measurements to be made in the field. Inverse modeling serves as an alternative approach to

61 recover soil properties using a combination of indirect and direct measurements and physics-based

62 numerical models.

63 Different inverse modeling frameworks have been developed to estimate soil thermal properties

64 using physical-based models and time-series of ground temperature data. Some earlier studies

65 used heat equation models without phase change (Beck et al., 1985; Allifanov et al., 1996). More

66 recent works include phase change, which is an important component of the energy balance in

67 permafrost-affected soils (e.g. Nicolsky et al., 2007; 2009, Tran et al., 2017). Nicolsky et al.,

68 (2007; 2009) used an optimization based inverse method and a variational data assimilation

69 method to estimate soil properties. In particular, Nicolsky et al., (2007; 2009) used measured

70 subsurface temperatures to inversely estimate thermal conductivities, porosities, freezing point

71 temperatures, and unfrozen water coefficients, pointing out that sensitivity analyses (i.e.

72 perturbation of the parameter values) are required in order to robustly establish a set of estimated

73 parameters. Harp et al., (2016) used an ensemble-based method to evaluate the uncertainty of

74 projections of permafrost conditions in a warming climate due to uncertainty in subsurface

75 properties. Atchley et al., (2015) used data calibration to estimate hydrothermal properties of soils.

76 All these methods used ground temperatures alone to estimate soil properties and 1D soil columns

77 assuming a 1D soil structure.

78 Recently, Tran et al., (2017) used a coupled hydrological–thermal–geophysical modeling approach

79 to estimate soil organic content. The approach was based on coupling the 1D Community Land

80 Model (CLM4.5; Oleson et al., 2013) that simulates surface-subsurface water, heat and energy

81 exchange and the 2D Boundless Electrical Resistivity Tomography (BERT) forward model

82 (Rücker et al., 2006). The simulated 1D snapshots of the subsurface temperature, liquid water and

83 ice content from the CLM model were explicitly linked to soil electrical resistivities via

84 petrophysical relationships which were then used as input to BERT's forward model to calculate

85 apparent resistivities. Their inverse modeling framework aims to minimize the misfit between

86 calculated and measured data, including soil temperature, liquid water content and apparent

87 resistivity. Here we modify and extend this approach to 2D by using the Advanced Terrestrial

88 Simulator (ATS) model, which was specifically developed to study fine-scale hydrothermal

89 processes of permafrost-affected soils. In addition, instead of estimating organic content of the soil

90 as in Tran et al., (2017), we estimate porosities and thermal conductivities of peat (organic) and

91 mineral layers across a 2D transect within polygonal tundra.

92   Modeling the full, continuous 2D transect allows us to simulate lateral hydro-thermal fluxes not

93   possible with individual 1D columns known to be important in polygonal tundra (Abolt et al, 2018,

94   Liljedahl et al, 2016). At each grid cell in the transect, a physical state develops during the ATS

95   simulation (temperature, saturation, etc.) that is then used to calculate heterogeneous electrical

96   resistivities via petrophysical relations. This allows more realistic simulated apparent resistivities

97   that include the effects of lateral hydrothermal connectivity within the transect.

98   Through this approach, we develop a parameter estimation (PE) algorithm that aims to estimate

99   porosities and thermal conductivities in permafrost-affected soils through joint inversion of

100   hydrothermal and geophysical measurements, including ground temperature, saturation, and

101   apparent resistivity. Our main objective then is to evaluate which types and number of

102   measurements are necessary to constrain the inversion to yield a robust and accurate prediction of

103   subsurface porosities and thermal conductivities. The inverse modeling framework couples the

104   state-of-the-art hydrothermal permafrost simulator ATS, electrical resistivity software package

105   BERT and the Model Independent Parameter Estimation and Uncertainty Analysis toolbox (PEST)

106   software package (Doherty, 2001). We progressively test the accuracy and robustness of the

107   method using a series of synthetic problems by: 1) increasing the complexity of the meteorological

108   data used to drive the coupled thermo-hydro-geophysical model and 2) testing the inclusion of

109   individual and combinations of several available measurement types on the accuracy and

110   robustness of inversions. The results of this work can be used to better understand challenges

111   associated with subsurface porosity and thermal conductivity estimation. Additionally, we used

112   findings from this study to suggest how data should be collected to improve the accuracy of the

113   estimated soil properties and to optimize the total number of measurements needed to make a

114   robust subsurface PE.

115

116   **2. Methods**

117   We estimate the soil properties of porosity and soil grain thermal conductivity for peat and mineral

118   layers of a 2D transect within polygonal tundra. Our PE approach is summarized in Figure 1. Given

119   specified "true" values of these parameters, we used the ATS version 0.86 model to solve for a

120   transient, spatially distributed hydro-thermal state characterized by temperature and liquid and ice

121   saturations. ATS is a 3D-capable coupled surface and groundwater flow and heat transport model

122   representing the soil physics needed to capture permafrost dynamics, including flow of unfrozen

123   water in variably-saturated, partially-frozen, non-homogeneous soils (Painter et al., 2016). Given
124   this hydrothermal state, we calculate resistivity values at every grid cell via petrophysical
125   relationships, and run the forward modelling component of the BERT software package (Rücker
126   et al., 2006) to simulate resistance and related apparent resistivity values that would be measured
127   with ground-coupled electrodes and an ERT acquisition system.

128
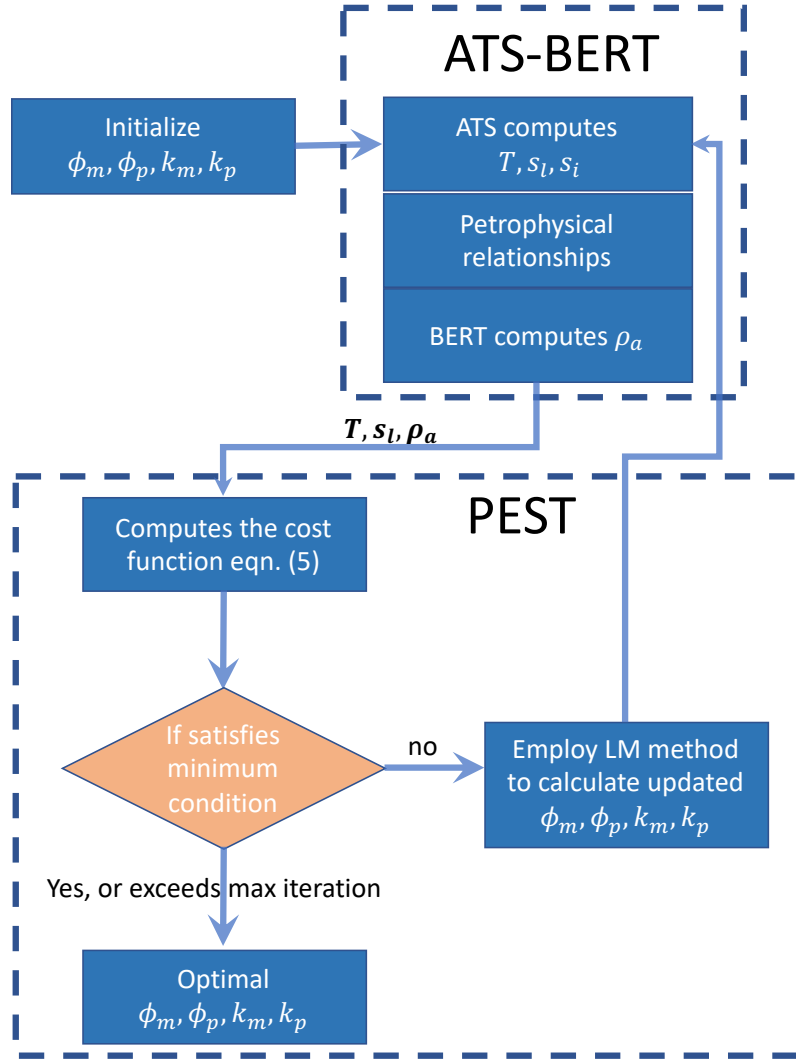
129 **Figure 1.** Schematics of the parameter estimation algorithm. The algorithm starts with initial guesses on
130 porosities and thermal conductivities $\{\phi, k\} = \{\phi_m, \phi_p, k_m, k_p\}$ for the peat and mineral layers. The coupled
131 ATS-BERT forward model then simulates temperature, liquid water, and apparent resistivities, which are
132 passed to the cost function. If the cost function is small enough, $\{\phi, k\}$ are considered to be the estimated
133 parameters. If not, the values of the $\{\phi, k\}$ are updated according to the Levenberg-Marquardt (LM)
134 minimization algorithm and passed back to the ATS-BERT model.

135

136 **2.1 ATS-BERT Model**

137 To set up the synthetic model, we used digital elevation data of a transect through ice-wedge

138 polygonal tundra at the Barrow Environmental Observatory (BEO), at Utqiagvik, Alaska (Fig. 2).

139 Our study includes an 11 m section covering a single polygon with an ice-wedge on each side. In

140 this study we do not explicitly assign ice properties for the ice-wedges. Instead, we model bulk

141 porosities and effective thermal conductivities that can be associated with peat and mineral layers

142 of the entire transect.

143 In Figure 2A, we present the computational mesh representing the cross-section of the polygonal

144 tundra that ATS is run on. The thickness of the peat layer corresponds to observations at the site,

145 with a thick peat layer on the sides (troughs) and thinner in the middle of the low-centered polygon.

146 A mineral layer was assigned below the peat layer across the transect. We initially designated six

147 synthetic direct temperature and soil moisture measurement locations within the active layer area,

148 the maximum thaw layer from the ground surface to the top of the permafrost, similar to the sensor

149 setup at the site (Dafflon et al., 2017). The average active layer depth is about 38cm, as it can be

150 seen from the ground temperatures simulated for the synthetic model run with actual

151 meteorological data in Figure 2B. The linear white region on Fig. 2B indicates the bottom of the

152 active layer within the transect (0° C). Then we added four more synthetic direct measurement

153 locations below the active layer to evaluate the effect of their inclusion on PE accuracy and

154 robustness. All observation locations are represented as stars on Figure 2A corresponding to the

155 locations of the collected daily averaged temperature and soil moisture timeseries.   The

156 temperature and soil moisture timeseries were recorded at depths of 5, 20, 60, and 80 cm below

157 the surface.

158 The setup of the ATS model followed a standard procedure described in several studies (Atchley

159 et al., 2015; Painter et al., 2016; Jafarov et al., 2018). Typically, we set up the model in several

160 steps: 1) initialization of the water table, 2) introduction of the energy equation to establish

161 antecedent permafrost, and 3) spinup of the model with simplified and actual meteorological data

162 from the BEO station. We spun up the model until the active layer achieved cyclical equilibrium.

163 The overall depth of the modeling domain is 50 m. We set the bottom boundary to a constant

164 temperature of T=263.55K and set zero heat and zero mass flux boundary conditions on the vertical

165 sides. A seepage face was imposed at 4 cm below the surface on each side of the domain to allow

166 drainage to the trough network to prevent water from pooling at the surface, as is typical of partially

167 degraded polygonal ground (Liljedahl et al, 2016). We use two types of meteorological datasets

168   as surface boundary condition drivers for the ATS model: simplified (sinusoidal air temperature,

169   constant precipitation, and constant radiative forcing) and actual weather data from the BEO site.

170   The actual meteorological data were collected starting on January 1, 2015 and include air

171   temperature, rain and snow precipitation, humidity, long and shortwave radiation, and wind speed.

172   We created a synthetic truth by designating porosities and soil grain thermal conductivities $\{\phi, k\}$

173   of peat and mineral soil as parameters in the forward model. The resulting temperature (T), liquid

174   and ice-water saturations (s_l, s_i), and apparent resistivities (ρ_a) were collected as the true state.

175   Critical for these simulations is the calculation of the thermal conductivities of the bulk soil;

176   calculated in ATS using Kersten numbers to interpolate between saturated frozen, saturated

177   unfrozen, and fully dry states (Painter et al., 2016) where the thermal conductivities of each end-

178   member state is determined by the thermal conductivity of the components (soil grains, air, water,

179   or liquid) weighted by the relative abundance of each component in the cell (Johansen, 1977;

180   Peters-Lidard et al, 1998; Atchley et al., 2015). Thermal conductivities of water, ice, and air are

181   considered constant, leaving soil grain thermal conductivity as the remaining parameter to be

182   estimated. The equation to calculate saturated, frozen thermal conductivity ($\kappa_{sat,f}$) has the

183   following form:

184 $$\kappa_{sat,f} = \kappa_{sat,uf} \cdot \kappa_i^{\phi} \cdot \kappa_w^{-\phi}, \tag{1}$$

185   where $\kappa_{sat,uf}$, κ_i, κ_w are thermal conductivities for saturated unfrozen, ice, and liquid water,

186   respectively, and ϕ is porosity.

187   The freezing characteristic curve is thermodynamically derived using a Clapeyron relation and the

188   unfrozen water retention curve, as described in Painter and Karra (2014) and Painter et al., (2016).

189   In Figure 3 we present liquid and ice saturations for one realization of the model for winter

190   (January) and summer (August) times of the year. The ice saturation is high below the active layer

191   all year long and lowest within the active layer in the summer. The peat layer holds more water;

192   therefore, ice concentration is higher than in the mineral layer in the winter. The liquid saturation

193   plot shows that by the end of the summer, the peat layer is drier than the mineral layer.

194   We sequentially couple the ATS and BERT numerical models via petrophysical relationships used

195   by Tran et al. (2017) and based on Archie (1942) and Minsley et al. (2015). In that approach, the

196   electrical resistivity (ρ) is determined as a function of soil characteristics, temperature, porosity,

197   liquid water saturation, fluid conductivity, and ice content:

198 $$\rho = 1/(\phi^d [s_l^n \sigma_w + (\phi^{-d} - 1)\sigma_s] \cdot [1 + c(T - 25)]), \tag{2}$$

199 where σ_w is the fluid electrical conductivity, σ_s is soil/sediments electrical conduction, n is a

200 saturation index, d is a cementation index, and c is a temperature compensation factor accounting

201 for deviations from $T = 25^o C$.

202 The ice content is linked to water content through the liquid-water saturation and to σ_w, which is

203 influenced by the concentration of Na^+ and Cl^- ions and the ice/liquid fraction. Here σ_w has the

204 following form:

205
$$\sigma_w = \sum_{i=1}^{n_{ion}} F_c \beta_i |z_i| C_{i(S_{f_{i=0}})} S_{fw}^{-\alpha} \tag{3}$$

206 Where F_c is Faraday's constant, β_i and z_i the ionic mobility and valence respectively, C_i is the

207 concentration of ith ion, α is factor influencing how the liquid water salinity increases when the

208 fractions of liquid in ice-liquid water S_{fw} decreases. S_{fw} is defined as:

209
$$S_{fw} = s_l/(s_l + s_i) \tag{4}$$

210 Both s_l and s_i are simulated by ATS. Note that ϕ in eq. (2) is an estimated parameter (see

211 Figure 1). In this study we assume that $n, d, \sigma_s, \alpha, F_c, \beta_{Na^+}, \beta_{Cl^-}, C_{Na^+}$, and C_{Cl^-} parameters used

212 in equations (2) and (3) are known (see Tran et al., 2017) and focus on the robustness of the PE

213 algorithm in estimating porosity and thermal conductivity.

214 The 2D resistivity data inferred from ATS simulations and petrophysical relationships gets

215 passed to BERT which simulates resistances that are then converted to ρ_a. The ρ_a values

216 correspond to an acquisition along an 11 m long transect using a 0.5 m electrode spacing and a

217 Schlumberger configuration with a total of 138 measurements (see Fig. 2B). This configuration

218 implies that the measurements are mostly sensitive to the electrical resistivity in the top few

219 meters.

220 Since BERT and ATS operate on different unstructured meshes, we wrote a function that

221 interpolates the values between the two meshes. Note that the ATS mesh is 50m deep. We

222 calculate ρ by using corresponding outputs from the ATS model and the petrophysical

223 relationships and then interpolated on a mesh defined in BERT and adapted to the acquisition

224 geometry. BERT's mesh consists of a finely resolved mesh (11m wide by 4.5m deep) embedded

225 eithin a coarser outer mesh that is about 120m wide and 85m deep. We link hydrological

226 variables with electrical resistivities in the fine mesh. The coarse mesh is used to reduce the

227 effect of boundaries. It extends until the change in the electrical resistivity between two

228 neighboring cells is negligible.

229
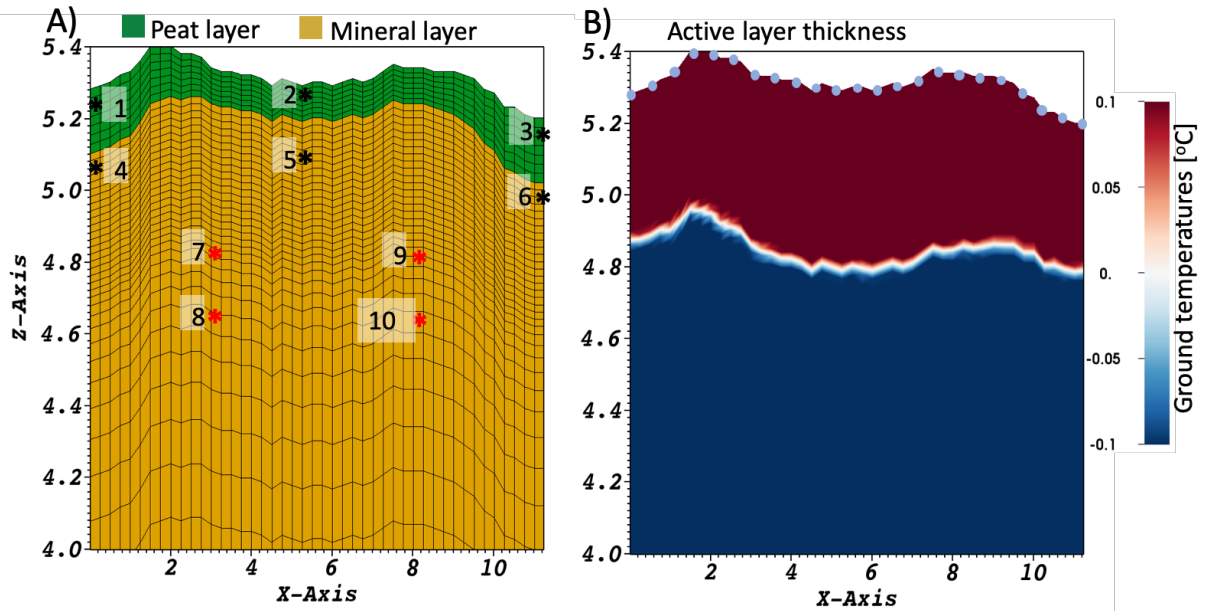
Figure 2. The (vertically exaggerated) 2D transect used by ATS model. A) The unstructured mesh where green represents the peat layer and brown represents the mineral soil layer. Black stars represent the 6 sensors recording temperature and soil moisture content within the active layer. Red stars represent the 4 sensors recording temperature and soil moisture content below the active layer. B) Ground temperature distribution simulated by the ATS model, corresponding to the time of maximum active layer depth. Here the depth of the active layer corresponds to the distance above the white linear feature (i.e., 0°C) dividing the thawed and frozen regions of the ground. The light blue dots represent the location of the electrodes in this setup.

238
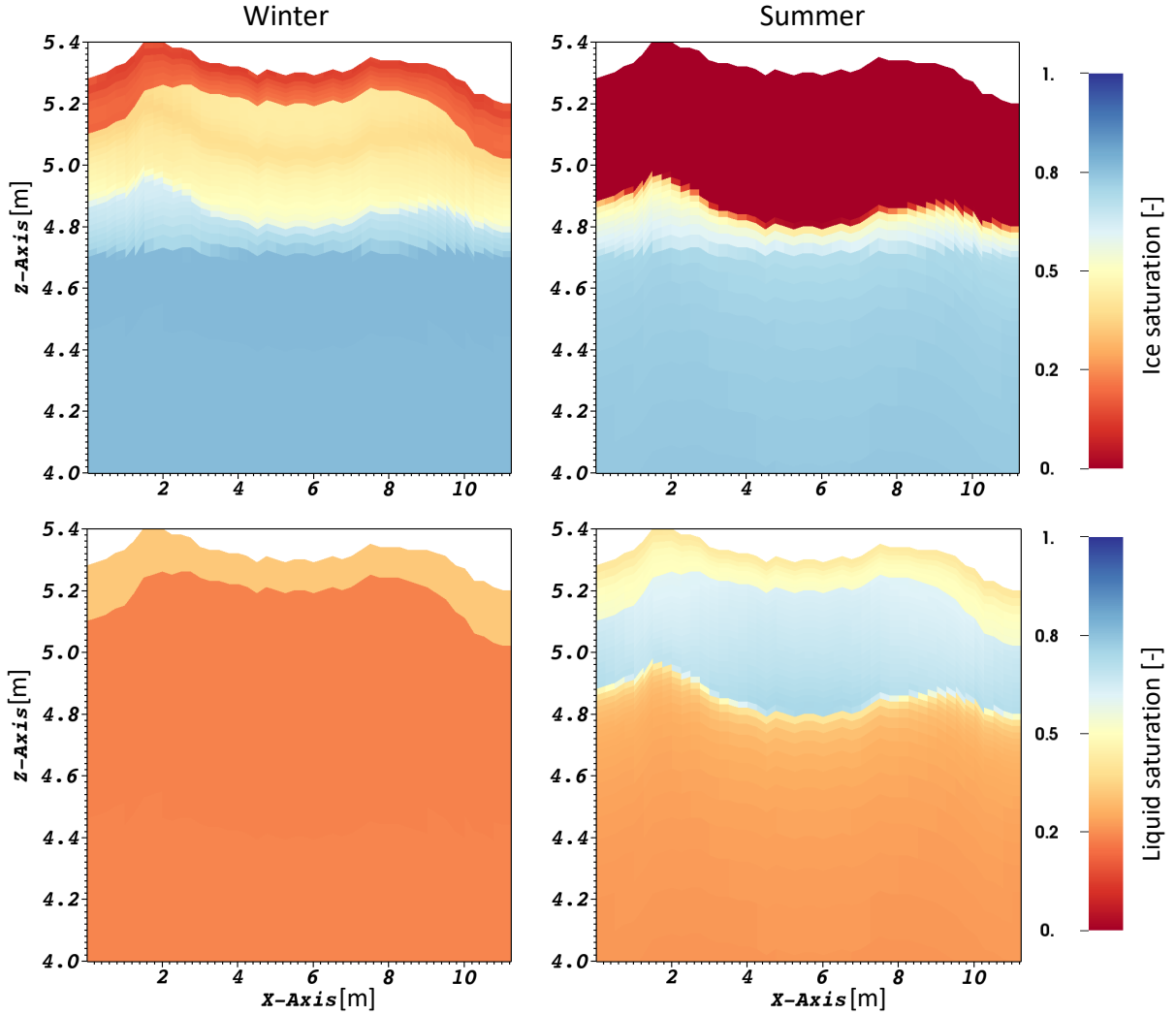
Figure 3. The 2D transect used by the ATS model. The rows from top to bottom correspond to liquid and ice saturation, respectively. The columns from left to right indicate a one-day snapshot taken in the middle of the winter and one-day snapshot over the summer corresponding to the maximum active layer depth day.

2.2 Parameter estimation using PEST

To test if the known soil properties can be recovered by the PE approach, we start with randomly selected initial parameter guesses. We use a Latin Hypercube Sampling method to generate random initial guesses of porosity and thermal conductivities around the synthetic truth (McKay et al., 1979). Each parameter combination includes four parameters: porosity and thermal conductivity for peat and mineral soil layers. The rest of the hydrothermal properties are kept fixed. These parameters were chosen due to their strong controls on both hydrologic and thermal states (Atchley et al., 2015, Nicolsky et al., 2009).

253   The inverse approach involves the minimization of a cost function expressed as the sum-of-squared

254   differences between simulated values and synthetic measurements using the Levenberg-Marquardt

255   (LM) algorithm (K. Levenberg, 1944; D. W. Marquardt 1963) implemented in the PEST software

256   package (Doherty, 2001), which was used to handle all parameter estimation runs.

257   To estimate soil porosities and thermal conductivities, we minimize the cost function (J), which

258   includes the calculated and synthetic T, s_l, and ρ_a in the following form:

$$J(\phi, k) = w_T \sum_i^{n_{sens}} \sum_j^{n_{days}} \left(T_{cj}^i - T_{sj}^i\right)^2 + w_s \sum_i^{n_{sens}} \sum_j^{n_{days}} \left(s_{l\,cj}^i - s_{l\,sj}^i\right)^2 +$$

259

$$w_{\rho_a} \sum_k^{n_{snap}} \sum_m^{n_{meas}} \left(\rho_{a\,cm}^k - \rho_{a\,sm}^k\right)^2, \tag{5}$$

260

261   where subscripts c and s correspond to calculated and synthetic states of the system, w_T, w_s, and

262   w_{ρ_a} are the corresponding weights for the temperature, saturation and apparent resistivity

263   residuals. n_{sens} is the number of sensors, n_{days} is the number of days over which we collected the

264   data, n_{snap} is the number of ρ_a snapshots, and n_{meas} is the number of ρ_a measurements during

265   one snapshot. T_c and s_{l_c} are timeseries from multiple sensors collected daily from the beginning

266   of June till the end of September. ρ_a are apparent resistivity data snapshots taken at a certain day.

267   The number of apparent resistivity snapshots depends on the particular case, varying from one to

268   eight snapshots per year. The one-snapshot case corresponds to only one snapshot in the month

269   of August while the eight-snapshot case corresponds to a snapshot taken once per month from

270   January till September. In addition, we tested the case where we collected eight daily ρ_a snapshots.

271   This was done to compare how different time spacing would affect the estimated properties.

272   The weights were chosen in order to scale the contribution of each type of residual so that

273   contributions to the cost function are evenly distributed across temperature, saturation, and

274   apparent resistivity residuals. For example, saturation residuals are on the order of a few tenths,

275   while apparent resistivity residuals can be tens of ohms. The weights were selected based on

276   evaluating the individual contributions to the cost function for each measurement type on an

277   ensemble of simulations spanning the parameter ranges. The apparent resistivity residual weight

278   (w_{ρ_a}) was set to one. The temperature and saturation residual weights (w_T and w_s) were then

279   modified so that each measurement type component in the cost function had roughly equivalent

280   magnitude over most of the parameter space. This resulted in weights of $w_{\rho_a} = 1$, $w_T =$

281    $\sqrt{2.5 \cdot 10^3}$, and $w_s = \sqrt{3.5 \cdot 10^5}$.

282   If the cost function satisfies minimum criteria or the maximum allowed number of iterations, which

283   we chose to be equal to 25, is reached, the PE terminates. The porosities and thermal conductivities

284   corresponding to the minimum of the cost function, i.e., the parameters associated with the best fit

285   between simulated and synthetic values, are considered the estimated parameter values as

286
$$\{\phi, k\} = \underset{\substack{\phi_{min} \leq \phi \leq \phi_{max,} \\ k_{min} \leq k \leq k_{max}}}{\operatorname{argmin}} J(\phi, k), \tag{6}$$

287   here $\{\phi, k\}$ are estimated porosities and thermal conductivities for peat and mineral soil.

288   Based on sensitivity analyses using simplified meteorological data, the cost function response

289   surface was smooth and convex over the parameter ranges of interest. Therefore, we chose the LM

290   approach because of its robust gradient-based optimization scheme that takes advantage of smooth

291   convex response surfaces to quickly converge to minima.

292   To build an understanding of the inverse framework, we start with a simple setup and then

293   gradually add more complexity. First, we use simplified meteorological data where we assume

294   that air temperatures change according to a sinusoidal function and all other terms are constants.

295   Initially we started with 3 temperature and moisture content measurement locations within the peat

296   layer (refer to Figure 2A) and 1 ERT data snapshot. Then we increase the number of ERT data

297   snapshots up to 8 by adding snapshots once per month from January till August. Each ERT data

298   snapshot calculated by BERT uses the set of daily averaged T and s_l simulated by ATS and

299   petrophysical relations (eqns. 2 and 3) which are varying over time. Then we increase the number

300   of sensors to 6 and add noise to the simulated data. Introduction of the noise allows us to evaluate

301   the effect of measurement uncertainties that will be present in the actual application of the PE

302   method. We added different levels of Gaussian noise to the synthetic measurements of T, s_l, and

303   ρ_a in the following way: 1% to T, 5% to s_l, and 10% to ρ_a. These levels of noise for the different

304   types of measurements are based on published literature and our own experience (Wang et al.,

305   2018; Dafflon et al., 2017). After that we substitute simplified meteorological data with actual data

306   from the BEO site to evaluate our PE method under realistic ground surface boundary conditions.

307   In this case we evaluate how much and what kind of data we need to robustly recover subsurface

308   porosities and thermal conductivities. To do this we test the inclusion of individual types of

309   measurements in the cost function (equation 3) as well as all possible combinations of

310   measurement types. We used different soil property ranges for the simplified and actual

311   meteorological data PE runs which are summarized in Table 1. This was done to test the

312 consistency and effectiveness of the PE method. In addition, we compared the difference between

313 estimated parameters for 8 ERT data snapshots collected once a month for 8 months versus once

314 a day for 8 days. Notation and a description of each run for simplified and actual meteorological

315 data are summarized in Table 2.

316 **Table 1: Allowed range for the estimated parameters.**

Properties	Simplified meteorological data		Actual meteorological data	
	peat	mineral	peat	Mineral
Porosity $[m^3 \cdot m^{-3}]$	0.8±1.9	0.6+0.25	0.6±1.9	0.4+0.25
Thermal conductivity, $[W\ m^{-1}K^{-1}]$	0.225±0.2	2.0±0.5	0.15±0.1	1.6±0.5

317

318 **Table 2: Description of all PE cases used in this study**.

Case #	Simplified meteorological data (S)		Actual meteorological data	
	Case name	Description	Case name	Description
1	(S)$3T3s_l1\rho_a$	All data from #1 to #3 sensors, and 1 ρ_a snapshot	$6T$	Sensors from #1 to #6, temperature only
2	(S)$3T3s_l8\rho_a$	All data from #1 to #3 sensors, and 8 ρ_a snapshots	$10T$	Sensors from #1 to #10, temperature only
3	(S)$6T6s_l1\rho_a$	All data from #1 to #6 sensors, and 1 ρ_a snapshot	$6s_l$	Sensors from #1 to #6, liquid saturation only
4	(S)$6T6s_l8\rho_a$	All data from #1 to #6 sensors, and 8 ρ_a snapshots	$1\rho_a$	1 ρ_a snapshot on month of August
5	(S)$6T6s_l1\rho_a+n$	All data from #1 to #6 sensors, and 1 ρ_a snapshot with added noise	$6T1\rho_a$	Temperature sensors from #1 to #6, and 1 ρ_a snapshots
6	(S)$6T6s_l8\rho_a+n$	All data from #1 to #6 sensors, and 8 ρ_a snapshots with added noise	$6s_l1\rho_a$	Liquid saturation sensors from #1 to #6, and 1 ρ_a snapshots
7			$6T6s_l$	Temperature and liquid saturation sensors from #1 to #6
8			$3T3s_l1\rho_a$	All data from #1 to #3 sensors, and 1 ρ_a snapshot

9			$3T3s_l8\rho_a$	All data from #1 to #3 sensors, and 8 ρ_a snapshots
10			$6T6s_l8\rho_a$	All data from #1 to #6 sensors, and 8 ρ_a snapshots
11			$6T6s_l8\rho_a(s)$	All data from #1 to #6 sensors, and 8 ρ_a snapshots, taken every day
12			$6T6s_l1\rho_a$	Special case, we moved sensors #4, #5 and #6 below the active layer depth (at 80cm depth), and 1 ρ_a snapshot
13			$10T10s_l1\rho_a$	All data from #1 to #10 sensors, and 1 ρ_a snapshot
14			$10T10s_l8\rho_a$	All data from #1 to #10 sensors, and 8 ρ_a snapshots

319 The numbers before T and s_l correspond to the number of sensors used. Number before ρ_a corresponds
320 to the number of apparent resistivity snapshots used. n stands for noise added to the synthetic
321 measurements. (S) corresponds to runs driven by simplified meteorological data. (s) represents daily ρ_a
322 snapshots.

323

324 **3. Results**

325

326 **3.1 Simplified meteorological data**

327 To evaluate the PE method performance driven by simplified meteorological data, we ran PE

328 experiments using 30 different random combinations of porosity and thermal conductivity values

329 as the initial starting point. We used 30 PE samples of $\{\phi, k\}$ starting points in the first experiment

330 ((S)$3T3s_l1\rho_a$) to illustrate the overall performance of the parameter estimation using a large

331 number of samples. After that, we did only five PE runs for the simplified meteorological data and

332 10 for all other runs with actual meteorological data. For all figures after Figure 4, for consistency

333 and clarity, we show results for only five PE runs per case. It is important to note that the number

334 of samples that one needs to run to ensure the robust convergence of the estimated parameters

335 depends on the specifics of the corresponding case (i.e. experiment specific). If most of the LM

336 runs converge to the same set of parameters and have low cost function values, then that set of

337 runs most likely corresponds to the actual $\{\phi, k\}$. In Figure 4, the red triangles represent initial

338 guesses (parameter combinations). In these plots, the synthetic truth is indicated by the intersection

339 of the two dotted lines. Yellow lines connecting red triangles with white crosses represent the path

340 that the LM algorithm has taken from the initial guess to the estimated parameter combination

341 (white crosses, Fig. 4). The yellow dots along the yellow lines indicate the location at each LM

342 iteration. Figure 4 indicates that the method is able to recover porosities more robustly than

343 thermal conductivities, i.e. estimated porosities are similar to their true state. According to the

344 liquid saturation plot on Figure 3, liquid saturation of the mineral layer is quite dynamic and more

345 saturated in comparison to the peat layer. Nevertheless, thermal conductivity of the mineral layer

346 (k_m) corresponds to the highest mismatch. Three out of thirty inversions corresponding to k_m end

347 up close to 1.4 $W\ m^{-1}K^{-1}$ (the true value is 2 $W\ m^{-1}K^{-1}$), suggesting those values do not

348 correspond to the 'truth', since most of the estimated values (27 cases) are concentrated around

349 the intersection of the dotted lines. In this case the response surface for the corresponding cost

350 function (eqn. 5) lies in a flat, low-gradient region. The projections of the cost function response

351 surfaces corresponding to porosities (Figure 4A) has a better defined minimum, as opposed to

352 projections of the cost function response surfaces corresponding to thermal conductivities (Figure

353 4B), indicating non-uniqueness of the estimated parameters. Here, we recorded time-series of T

354 and s_l only from the first 3 near-surface sensors (Figure 2A). All of these 3 sensors are located in

355 the peat layer, suggesting that using just near-surface sensors only from one upper layer might not

356 be enough to recover the deeper layer thermal conductivity.

357
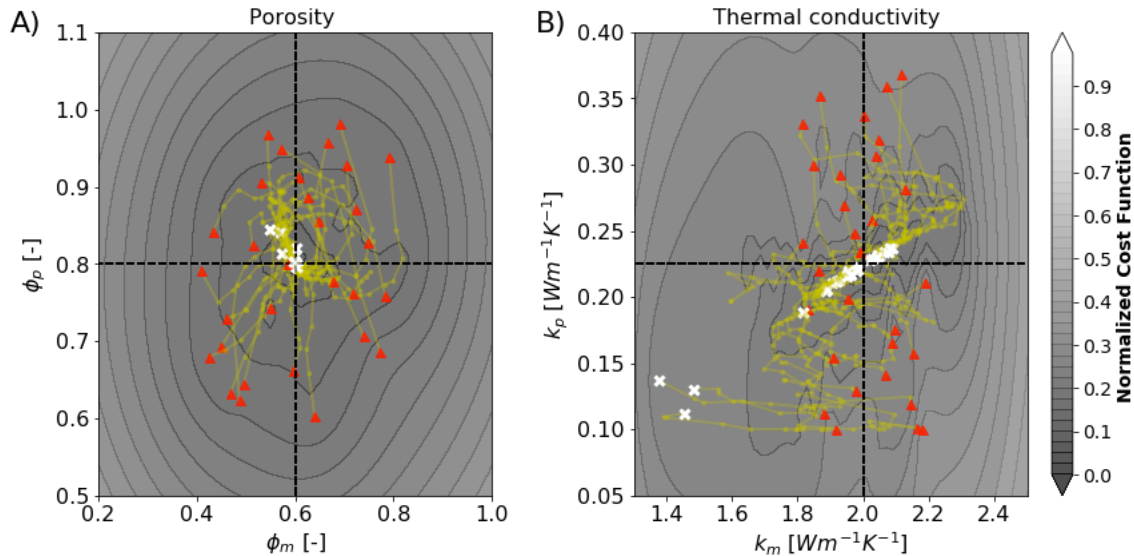
358 **Figure 4.** Estimated properties from 30 inversions of the (S)3T3s_l1ρ_a case, where the "true" values are
359 shown as a cross-section of two dashed lines for the bulk porosities and effective thermal conductivities
360 for peat and mineral soil layers. Yellow lines correspond to the paths taken by the LM algorithm. The
361 white dots correspond to the estimated values. A) projection of the cost function with respect to porosities
362 of peat and mineral layer. B) projection of the cost function with respect to thermal conductivities of peat

363 and mineral layer. The color bar represents the cost function normalized by its maximum logarithmic
364 value.
365

366 To illustrate the effect of noise on the robustness of the estimated parameters we used cases with

367 6 near-surface sensors ($6T$ and $6s_l$), and a varying number of ERT snapshots driven with simplified

368 meteorological data. Similarly to the (S)$3T3s_l1\rho_a$ case, (S)$6T6s_l1\rho_a$ shows good convergence

369 for porosities and poor convergence for thermal conductivities with an averaged error of

370 $0.1Wm^{-1}K^{-1}$ (Figure 5AB). Adding noise to the (S)$6T6s_l1\rho_a+n$ case slightly worsens the

371 estimated porosity values and significantly worsens k_m with root-mean-squared error (RMSE)

372 raising from 10% to more than 50% (Figure 5CD). Figure 5EF shows that increasing the number

373 of ERT snapshots from 1 to 8 per year (i.e. collected once per month from January till September)

374 improves k_m estimates, allowing better convergence for four out of five samples to the synthetic

375 truth. If we compare all three cases on Figure 5 on how well they are able to estimate k_m, it is

376 clear from Figure 5D that for the case (S)$6T6s_l1\rho_a+n$ none of the k_m's were correctly estimated.

377 Then by increasing the number of monthly ERT snapshots we significantly improved the estimated

378 values for k_m. Moreover, all except one estimated value showed a better match with its true value

379 than the (S)$6T6s_l1\rho_a$ case without any added noise.
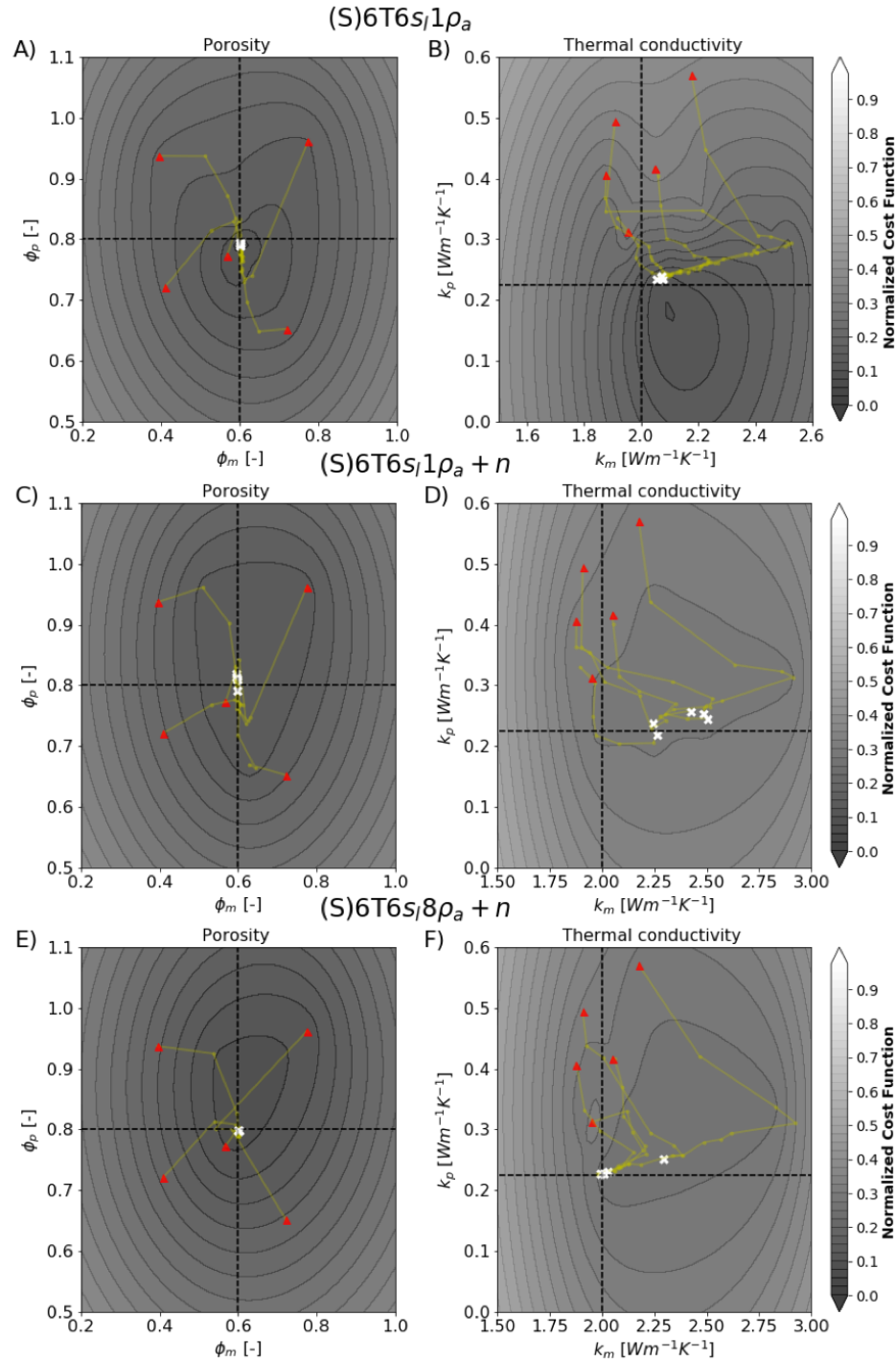
Figure 5. Estimated properties from 5 inversions of the three different cases, where the "true" values are shown as a cross-section of the two dashed lines for the bulk porosities and effective thermal conductivities for peat and mineral soil layers. Yellow lines correspond to the paths taken by the LM algorithm. The white dots correspond to the estimated values. The rows from top to bottom correspond to cases $(S)6T6s_l1\rho_a$, $(S)6T6s_l1\rho_a$+n, and $(S)6T6s_l8\rho_a$+n correspondingly. The columns from left to right correspond to the projection of the cost function with respect to porosities and thermal conductivities. The color bar represents the cost function normalized by its maximum logarithmic value.

389   In Figure 6, we summarize results of the five PE runs for each of the first six cases corresponding

390   to simplified meteorological data listed in Table 2. The first three matrix tables correspond to the

391   normalized RMSE values for each measurement type (ΔT, Δs_l, and $\Delta \rho_a$). The last two matrix

392   tables correspond to the normalized Euclidian distances between the synthetic truth and estimated

393   parameter values of $\delta \phi$ and δk. We normalized the values in each matrix by dividing by the

394   maximum value from the corresponding matrix. The normalized values are marked with tildes

395   and range from 0 to 1, where values closer to 0 correspond to a better match and values closer to

396   1 correspond to a worse match. As shown above, the method is able to accurately estimate both

397   peat and mineral soil porosities and peat layer thermal conductivity (k_p) but cannot always

398   accurately estimate k_m. There is not much difference between cases (S)$3T3s_l1\rho_a$ and

399   (S)$6T6s_l1\rho_a$ except for a slight improvement in k_m, suggesting that the small vertical distance (10

400   cm) between sensors 1 and 4, 2 and 5, and 3 and 6 could be limiting recorded data variability,

401   leading to difficulty in estimation of the k_m parameter. Since all 6 sensors lie within the active

402   layer zone, in the later experiments we added additional sensors below the active layer (red stars

403   in Figure 2A). The ϕ and k matrix tables show that increasing the number of monthly ERT

404   snapshots consistently improve the estimates of ϕ and k. This suggests that by increasing the

405   number of monthly ERT snapshots can lead to improved convexity of the cost function (eqn.5).

406

407
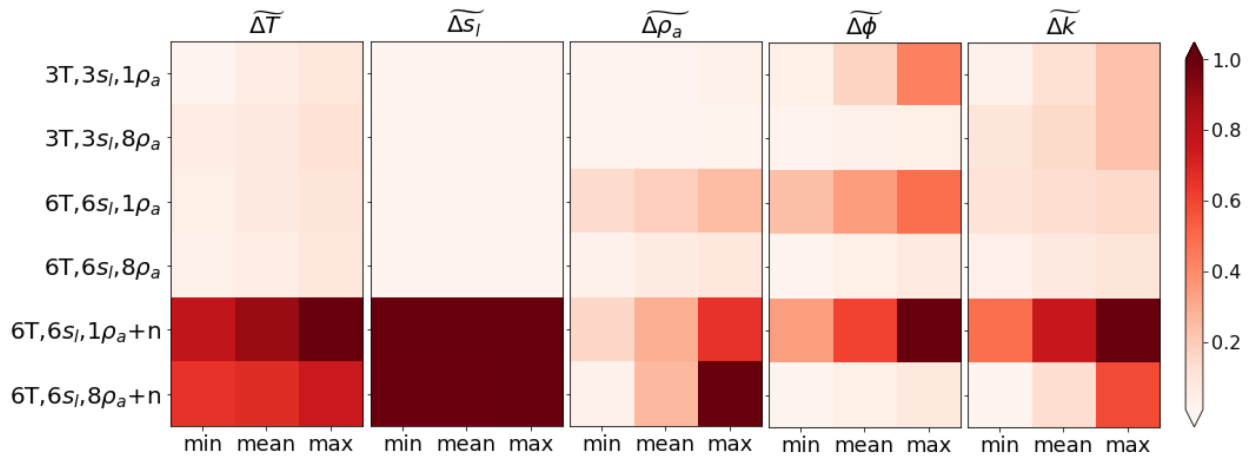
408   **Figure 6.** Five matrix tables presenting fitness metrics between synthetic model values and values
409   obtained by the parameter estimation method using simplified meteorological data. Matrix tables from left
410   to right correspond to the normalized root mean squared errors for temperatures, liquid water saturations,
411   and apparent resistivities and to the normalized Euclidian distances between synthetic ("true") and
412   estimated porosity, and thermal conductivity values. Each matrix value was normalized by dividing it by
413   the matrix maximum value. The normalized values are indicated by tildes.
414

3.2 Meteorological data from Utqiagvik (Barrow) site 2015

After testing the PE method for the simplified meteorological data, we applied measured meteorological data from the BEO site for year 2015. To better understand the importance of each measurement type and their combinations within the developed PE algorithm we tested all of the scenarios corresponding to the 'actual meteorological data' column from Table 2. The results of these runs are summarized in the colored matrix tables in Figure 7. Since there are more than twice the number of actual meteorological cases than the simplified meteorological cases, it is hard to analyze all matrix tables at once.

To compare the match between estimated and observational values on the same plot we calculated Euclidean norms for each case independently:

$$\Delta\left(\widetilde{\Delta T}, \widetilde{\Delta s_l}, \widetilde{\Delta \rho_a}\right)_i = \sqrt{\left(\frac{\Delta T_i}{\Delta T_{max}}\right)^2 + \left(\frac{\Delta s_{l_i}}{\Delta s_{l_{max}}}\right)^2 + \left(\frac{\Delta \rho_{a_i}}{\Delta \rho_{max}}\right)^2} \qquad (7)$$

$$\Delta\left(\widetilde{\delta \phi}, \widetilde{\delta k}\right)_i = \sqrt{\left(\frac{\delta \phi_i}{\delta \phi_{max}}\right)^2 + \left(\frac{\delta k_i}{\delta k_{max}}\right)^2} \qquad (8)$$

The index *i* indicates the case number (see Table 2). Then we applied k-means clustering analysis to group cases on how well they match data vs. estimated parameters. We divided all cases into four classes shown in Figure 8. Class I indicates the best cases that provide an accurate parameter estimation as well as accurate matches with the synthetic "true" measurements. Class II includes the cases that have accurate parameter estimates and less accurate matches with the measurements. Class III indicates all cases that have less accurate parameter estimates but accurate matches with the measurements. Finally, Class IV includes the cases that showed the worst performance in terms of parameter estimates and the worst matches with the measurements. We summarized the results from Figure 8 in Table 3.

Class I (see Table 3) suggest that sensors located below the active layer lead to better PE as well as increasing the number of sensors leads to more accurate parameter estimation. In contrast, Case #4 corresponding to the one ERT snapshot ($1\rho_a$), suggests that one ERT data snapshot could be enough for parameter estimation while Class II indicates that increasing the number of monthly ERT snapshots is important for more accurate PE. However, increasing the number of monthly ERT snapshots leads to a less accurate match with measurements. These results are consistent with the results for simplified data with added noise (Figure 5).

443 Class III includes 6 cases suggesting that if we have only soil moisture data available for PE, then
444 we should expect less accurate soil property estimates. The last element in this class suggests that
445 taking daily ERT snapshots improves the apparent resistivity match (Figure 7, resistivity table) but
446 does not improve $\{\phi, k\}$ estimates, where monthly ERT snapshots improve thermal conductivity
447 convergence.

448 Class IV once again clearly indicates that measurements obtained below the active layer provide
449 more accurate parameter estimates, however, they do not improve matches to measurements. This
450 is mainly due to significant mismatch with ρ_a, which can be seen from the $\widetilde{\Delta\rho_a}$ matrix table on
451 Figure 8. At the actual site, the depth to the mineral soil can be deeper than 20 cm, not having
452 sensors lower than 20 cm limits the amount of data that can help to improve the convexity of the
453 cost function in our case.

454 **Table 3:** K-mean analysis of the accuracy for each 13 cases.

Class I	Class II	Class III	Class IV
$10T\,10s_l\,1\rho_a$	$6T\,6s_l\,8\rho_a$	$6s_l$	$10T$
$10T\,10s_l\,8\rho_a$	$3T\,3s_l\,8\rho_a$	$6s_l\,1\rho_a$	$6T$
$1\rho_a$		$6T\,1\rho_a$	
$6T\,6s_l\,1\rho_a$		$3T\,3s_l\,1\rho_a$	
		$6T\,6s_l$	
		$6T\,6s_l\,8\rho_a(s)$	

455

456 From Figure 8 and Table 3 we know that the *6T* case has the worst performance in terms of
457 matching $\{\phi, k\}$. Similar to the experiments with simplified meteorological data, the main
458 difficulty for experiments with actual meteorological data is estimating thermal conductivity. The
459 last matrix table ($\widetilde{\delta k}$) on Figure 7 shows that $6T\,6s_l\,8\rho_a(s)$ has the highest maximum and mean
460 mismatch in thermal conductivity estimates. However, since ϕ estimates are a better match with
461 their corresponding "true" values, the case $6T\,6s_l\,8\rho_a(s)$ falls into class III in Figure 8, as opposed
462 to case *6T*, which falls into class IV. The highest mismatch in thermal conductivity values for the
463 $6T\,6s_l\,8\rho_a(s)$ case suggests that collecting daily ERT snapshots improves the ρ_a match (Figure 7,
464 $\widetilde{\Delta\rho_a}$ matrix table) but does not improve estimated parameters, where monthly ERT snapshots
465 improve thermal conductivity estimation.

466   To illustrate this, we plot values of estimated parameters and the corresponding response surfaces

467   of the cost function for cases $10T10s_l8\rho_a$ and $6T6s_l8\rho_a(s)$ on Figure 9. The PE method was able

468   to match 4 out of 5 estimates almost perfectly and missed the k_p for the $10T10s_l8\rho_a$ case. The

469   corresponding cost function has a visible minimum and clear convexity. In contrast to this, the

470    $6T6s_l8\rho_a(s)$ case completely missed 2 estimates by converging on values outside the boundaries,

471   and 3 other estimates do not converge to the desired cross section as well. The contour lines suggest

472   that the corresponding response surfaces of the cost function do not have a well-defined global

473   minimum.

474

475   **4. Discussion**

476

477   The existence of multiple minima is common in inverse modeling and can lead to false

478   convergence of the PE algorithm to physically non-realistic subsurface parameters (Nicolsky et

479   al., 2007). This is one of the main reasons for using multiple initial guesses. If most of the

480   inversions converge to a similar set of parameter estimates with the lowest cost function value,

481   then that set of values is most likely the global minimum. Testing the PE algorithm using multiple

482   starting points is a commonly used approach in evaluating the robustness of an inverse model (e.g.

483   P. Hansen, 1998).

484   A potential strategy to improve of the developed PE algorithms is to reduce the specified

485   convergence tolerance value (i.e. minimum condition, see Figure 1) or increase the allowable

486   number of iterations. However, this could lead to a significant increase in computational effort. In

487   addition, PEST provides multiple additional inverse settings to achieve a better convergence.

488   Parameter regularization is one of them. Regularization techniques have been widely used in

489   solving ill-posed inverse problems (Vogel, 2002). The overall idea is to constrain the objective

490   function by imposing additional priors on the estimated model parameters. We recognize that

491   including parameter regularization into the cost function may improve robustness of our method.

492   However, inclusion of the regularization would require an extensive exploration of the multiple

493   regularization methods and values that could be applied to it, which is beyond the scope of this

494   paper. Here we illustrate that without using regularization it is possible to achieve reasonable

495   results by using simple weighted cost function.

496   Good performance of the case with 1 ERT snapshot ($1\rho_a$) could be misleading due to the design
497   of this numerical experiment, i.e. we are using a synthetic "truth" produced by the same model
498   used in the inversion, which improves the convexity of the cost function and leads to a well
499   constrained unique minimum. However, in reality, collection of the additional information, such
500   as organic layer thickness and temperature data, are extremely important and are required for
501   model calibration (Jafarov et al., 2012; Atchley et al., 2015). In addition, real ERT surveys can be
502   perturbed by noise and their interpretation may require site-specific petrophysical relationships as
503   opposed to the general petrophysical relationships used in this study. Therefore, we do not suggest
504   inversion based on one ERT snapshot without any additional data.

505   The $6T6s_l8\rho_a(s)$ case, where all runs converge to different values of k_m, indicates that using
506   certain combinations of datasets does not allow the inverse approach to properly recover k_m. It is
507   likely that $6T6s_l8\rho_a(s)$ does not capture much variability in soil temperatures and soil moisture,
508   and therefore ERT snapshots do not have much variability as well. Once the cost function
509   converges for one of the ERT snapshots, it immediately converges on the other daily snapshots
510   due to their similarity. In fact, although $6T6s_l8\rho_a(s)$ has a good accuracy with observations (see
511   the $\widetilde{\varDelta\rho_a}$ matrix table in Figure 7), it is unable to recover the value of k_m.

512   We have shown that even in the ideal situation where we either generate observational data or use
513   simplified meteorological data, we cannot always fit modeling results to observations. In reality,
514   noise (e.g. the sensor's measuring resolution) influences the collected data. To investigate the
515   impact of measurement noise, we introduced multiple levels of noise to the simplified
516   meteorological data. The PE showed that dealing with noisy data could be challenging (Figure 5).
517   However, our results showed that adding monthly taken ERT snapshots into the cost function
518   improves the overall PE accuracy.

519   The distance between sensors could be another source of uncertainty in the PE. As it was pointed
520   out by Nicolsky et al., (2009), it is important to make sure that a vertical difference between
521   adjacent measurements do not introduce additional noise that can mislead the minimization
522   algorithm without providing new information. If sensors are close to each other, measurements
523   might be the same or within the noise variability. In our setup the vertical distance between the
524   first two rows of sensors is about 10cm. This could lead to small temperature variability between
525   sensors. Indeed, providing greater vertical distance between sensors improved the PE accuracy.

526   The Case #12 ($6T6s_l1\rho_a$) clearly illustrates this point, that by increasing the vertical distance

527   between sensors we can improve estimated parameter accuracy.

528   Combining hydrothermal observations from multiple depths with monthly ERT measurements

529   resulted in improving the shape of the cost function leading to better defined minima (Figure 9).

530   Increasing the number of the monthly ERT snapshots improved the accuracy of the estimated

531   parameters. In addition, we showed that having sensors below the active layer combined with ERT

532   snapshots shows the best accuracies both in terms of estimating parameters and matching

533   observations.

534

535   **5. Conclusion**

536   The overarching goal of this study was to develop and validate a PE algorithm using a synthetic

537   setup and 2D coupled thermal-hydro-geophysical model based on a polygonal tundra site within

538   the BEO.   Combining hydrothermal observations from multiple depths with monthly ERT

539   measurements resulted in an improved shape of the cost function and led to better defined minima

540   and improved accuracy of the estimated parameters. This was presented in fitness matrices for 6

541   cases using simplified meteorological data (Figure 6). Similar conclusion held for inversion runs

542   with actual meteorological data. It is important to note that it was not only the number of ERT

543   data snapshots that improved the robustness of the PE method but time frequency of the ERT data

544   snapshots, i.e. monthly vs daily snapshots. In addition, collecting data from several soil layers

545   might improve the thermal conductivity estimates for the corresponding soil layer.   Our

546   experiments show that robust PE can be achieved not just by adding more sensors into the ground

547   and increasing number of ERT snapshots, but also by optimally distributing those sensors within

548   the transect (e.g., the $6T6s_l1\rho_a$ case). Overall, the inversion runs that we investigated consistently

549   indicated that collecting data from multiple soils layers, providing enough vertical separation

550   between sensors, and collecting temporally diverse ERT data should lead to robust parameter

551   estimation. The exception from this conclusion is the case $1\rho_a$, which showed robust parameter

552   estimation due to specifics of the model setup. As discussed above, estimating porosities and

553   thermal conductivities based on 1 ERT snapshot would not be possible without additional

554   information on the subsurface properties.

555   This work developed and demonstrated the feasibility of a PE algorithm that can be used to better

556   inform large scale Land System Model subsurface parameterization. Here we demonstrated the

557   proof-of-concept of the PE method. Further improvements such as introduction of a PE

558   regularization parameter into the cost function and leveraging additional PEST capabilities could

559   improve method robustness. Finally, the PE method must still be tested using measured thermal-

560   hydro-geophysical data from the BEO site.

561
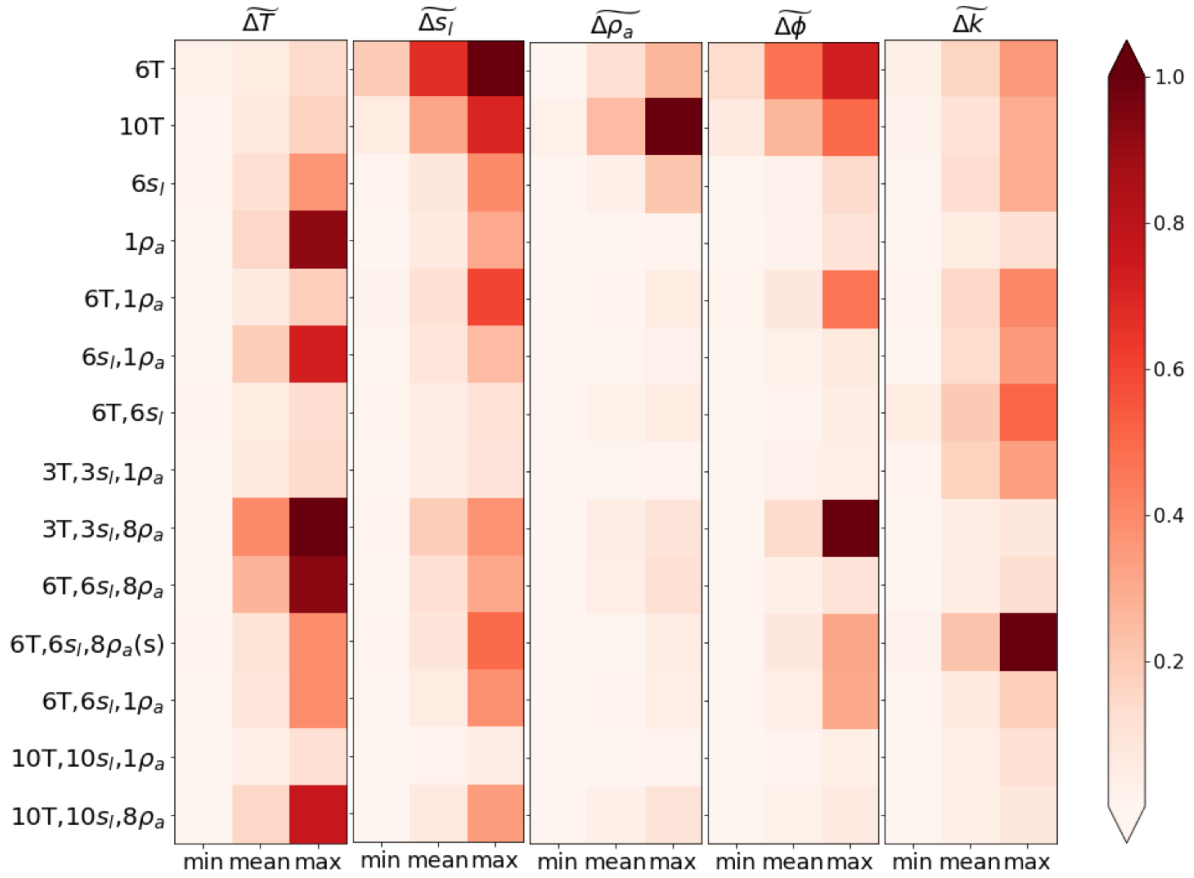
562 **Figure 7.** Five matrix tables presenting fitness metrics between synthetic model values and values
563 obtained by the parameter estimation method using meteorological data from year 2015 from BEO site in
564 Alaska. Matrix tables from left to right correspond to the normalized root mean squared errors for
565 temperatures, liquid water saturations, and apparent resistivities, and to the normalized Euclidian
566 distances between synthetic ("true") and estimated porosity, and thermal conductivity values. Each matrix
567 value was normalized by dividing it by the matrix maximum value. The normalized values are indicated
568 by tildes.
569

1, 6T
2, 10T
3, $6s_l$
4, $1\rho_a$
5, $6T1\rho_a$
6, $6s_l1\rho_a$
7, $6T6s_l$
8, $3T3s_l1\rho_a$
9, $3T3s_l8\rho_a$
10, $6T6s_l8\rho_a$
11, $6T6s_l8\rho_a(s)$
12, $6T6s_l1\rho_a$
13, $10T10s_l1\rho_a$
14, $10T10s_l8\rho_a$
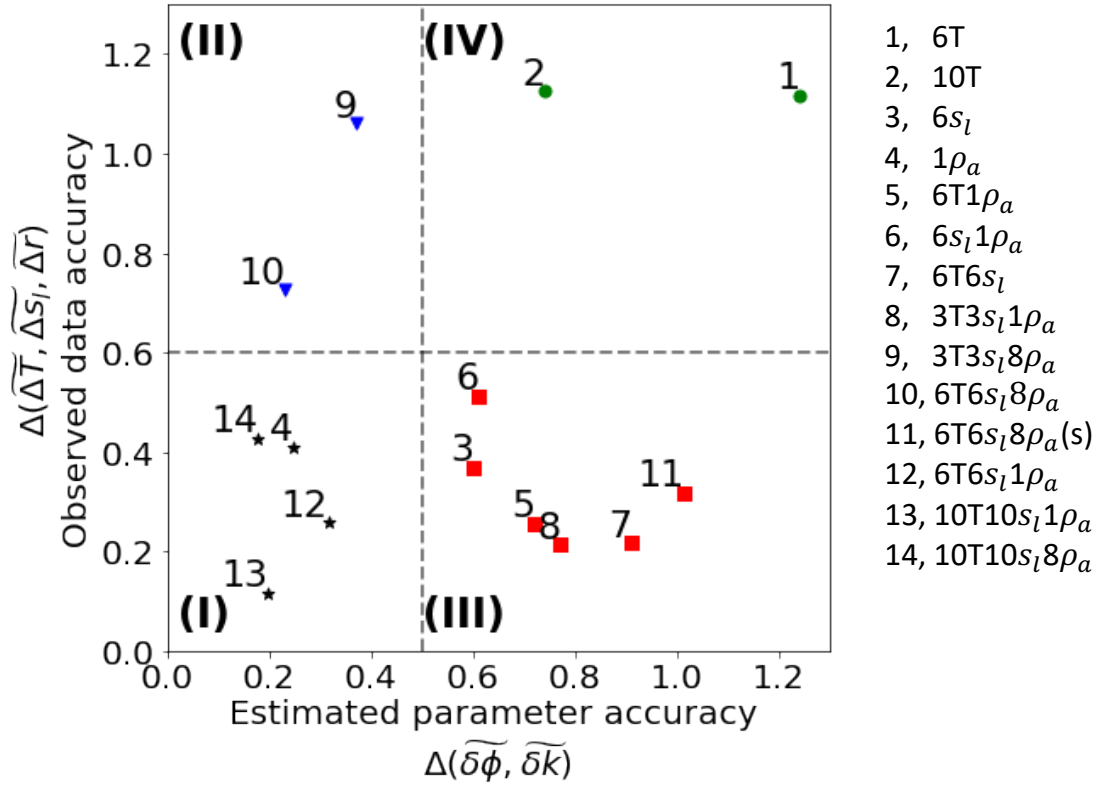
Figure 8. A k-means clustering analysis applied to the Euclidean norms of the normalized mean differences of estimated soil properties and the corresponding fit between calculated and observed values. Each color and marker represent a certain class as a result of the k-means clustering analysis.
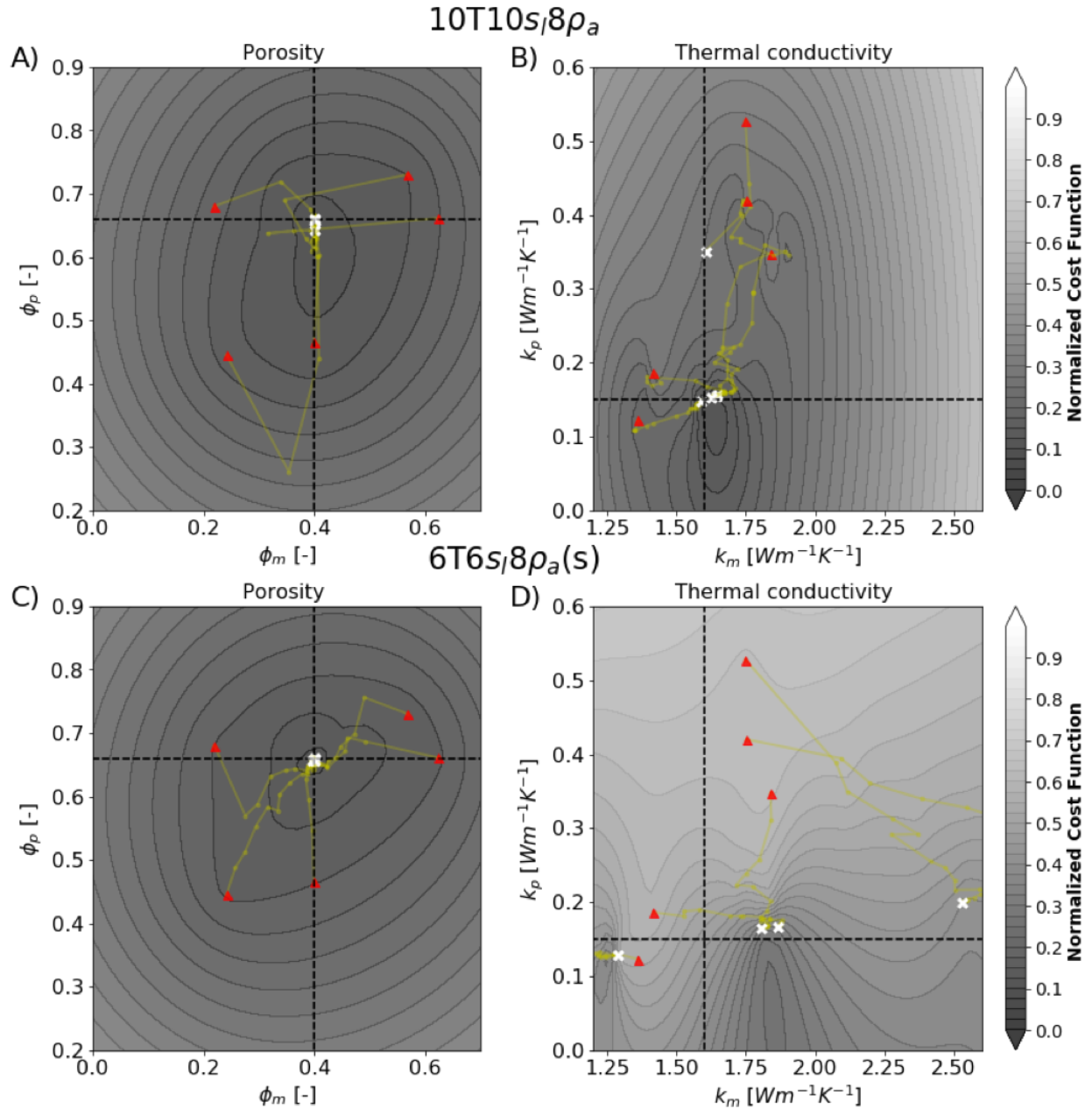
Figure 9. Estimated properties from 5 inversions of the two different cases, where the "true" values are shown as a cross-section of the two dashed lines for the bulk porosities and effective thermal conductivities for peat and mineral soil layers. Yellow lines correspond to the paths taken by the LM algorithm. The white dots correspond to the estimated values. The rows from top to bottom correspond to two cases: $10T10s_l8\rho_a$ and $6T6s_l8\rho_a(s)$. The columns from left to right correspond to the projection of the cost function with respect to porosities and thermal conductivities. The color bar represents the cost function normalized by its maximum logarithmic value.

5. Acknowledgements

This work is part of the Next-Generation Ecosystem Experiments (NGEE Arctic) project which is supported by the Office of Biological and Environmental Research in the DOE Office of Science.

6. References

Abolt, C. J., Young, M. H., Atchley, A. L., and Harp, D. R.: Microtopographic control on the ground thermal regime in ice wedge polygons, The Cryosphere, 12, 1957-1968, https://doi.org/10.5194/tc-12-1957-2018, 2018.

Alifanov, O., Artyukhin, E., Rumyantsev, S., 1996. Extreme Methods for Solving Ill-posed Problems with Application to Inverse Heat Transfer Problems. Begell House, New York.

Archie, G. E.: The electrical resistivity log as an aid in determining some reservoir characteristics, Society of Petroleum Engineers, T. AIME, 146, 54–62, 1942.

Atchley, A. L., Painter, S. L., Harp, D. R., Coon, E. T., Wilson, C. J., Liljedahl, A. K., and Romanovsky V.E.. 2015 Using field observations to inform thermal hydrology models of permafrost dynamics with ATS (v0.83) Geosci. Model Dev. 8 2701–22

Beck, J., Clair, C.S., Blackwell, B., 1985. Inverse Heat Conduction: Ill-Posed Problems. Wiley, New York.

Biskaborn et al., Permafrost is warming at a global scale, Nature Communications. 2019. Volume 10, Number1, Pages 264, https://doi.org/10.1038/s41467-018-08240-4.

Boike, J. and Roth, K.: Time domain reflectometry as a field method for measuring water content and soil water electrical conductivity at a continuous permafrost site, Permafrost Periglac., 8, 359–370, 1997.

Dafflon, B., Oktem, R., Peterson, J., Ulrich, C., Tran, A. P., Romanovsky, V., and Hubbard, S.: Coincident above and below-ground autonomous monitoring strategy: Development and use to monitor Arctic ecosystem freeze thaw dynamics, J. Geophys. Res.-Biogeo., 122, 1321–1342, https://doi.org/10.1002/2016JG003724, 2017.

Doherty, J., 2001. PEST-ASP user's manual. *Watermark Numerical Computing, Brisbane, Australia*.

Hansen, P. C., 1998. Rank-Deficient and Discrete Ill-Posed Problems: Numerical Aspects of Linear Inversion, Society for Industrial and Applied Mathematics (Publisher), pages 263. https://doi.org/10.1137/1.9780898719697.

617 Harp, D. R., Atchley, A. L., Painter, S. L., Coon, E. T., Wilson, C. J., Romanovsky, V. E., and
618   Rowland, J. C.: Effect of soil property uncertainties on permafrost thaw projections: a
619   calibration-constrained analysis, The Cryosphere, 10, 341-358, https://doi.org/10.5194/tc-
620   10-341-2016, 2016.

621 Hjort, J., Karjalainen, O., Aalto, J., Westermann, S., Romanovsky, V. E., Nelson, F. E.
622   Etzelmüller, B., and Luoto, M. Degrading permafrost puts Arctic infrastructure at risk by
623   mid-century. Nature Communications. 2018. Volume 9, Number1, Pages 5147,
624   https://doi.org/10.1038/s41467-018-07557-4.

625 Jafarov, E. E., Marchenko, S. S., and Romanovsky, V. E.: Numerical modeling of permafrost
626   dynamics in Alaska using a high spatial resolution dataset, The Cryosphere, 6, 613-624,
627   doi:10.5194/tc-6-613-2012, 2012

628 Jafarov, E. E., Coon E. T., Harp, D. R., Wilson, C. J., Painter, S. L., Atchley, A.L., Romanovsky
629   V. E.: (2018) Modeling the role of preferential snow accumulation in through talik
630   development and hillslope groundwater flow in a transitional permafrost landscape.
631   Environ. Res. Lett, 2018. https://doi.org/10.1088/1748-9326/aadd30.

632 Johansen, O. 1977. Thermal Conductivity of Soils No. CRREL-TL-637 Cold Regions Research
633   and Engineering Lab, Hanover NH

634 Kern, J. S.: Spatial Patterns of Soil Organic Carbon in the Contiguous United States, Soil Sci.
635   Soc. Am. J., 58, 439–455, 1994.

636 Koven, C. D., Riley, W. J., and Stern, A.: Analysis of permafrost thermal dynamics and response
637   to climate change in the CMIP5 earth system models, J. Climate, 26, 1877–1900,
638   https://doi.org/10.1175/JCLI-D-12–00228.1, 2013.

639 Levenberg, K.. A method for the solution of certain non-linear problems in least squares, Quart.
640   Appl. Math., 2 (1944), pp. 164–168. [28]

641 Marquardt, D. W.. An algorithm for least-squares estimation of nonlinear parameters, J. Soc. Ind.
642   Appl. Math., 11 (1963), pp. 431–441.

643 McKay, M.D.; Beckman, R.J.; Conover, W.J. 1979. A Comparison of Three Methods for
644   Selecting Values of Input Variables in the Analysis of Output from a Computer Code.
645   American Statistical Association. 21 (2): 239–245. https://doi.org/0.2307/1268522

646 McGuire A D et al 2018. The dependence of the evolution of carbon dynamics in the northern
647   permafrost region on the trajectory of climate change Proc. Natl Acad. Sci. 115, 3882–7

648   Minsley, B. J., Wellman, T. P., Walvoord, M. A., and Revil, A.: Sensitivity of airborne
649   geophysical data to sublacustrine and near-surface permafrost thaw, The Cryosphere, 9,
650   781–794, https://doi.org/10.5194/tc-9-781-2015, 2015

651   Nicolsky, D. J., Romanovsky, V. E., and Tipenko, G. S.: Using in-situ temperature
652   measurements to estimate saturated soil thermal properties by solving a sequence of
653   optimization problems, The Cryosphere, 1, 41-58, https://doi.org/10.5194/tc-1-41-2007,
654   2007.

655   Nicolsky, D.J., Romanovsky, V.E., Panteleev, G.G., 2009. Estimation of soil thermal properties
656   using in-situ temperature measurements in the active layer and permafrost. Cold Reg. Sci.
657   Technol. 55 (1), 120–129.

658   Painter, S. L., Coon, E. T., Atchley, A. L., Berndt, M., Garimella, R., Moulton, J. D., Svyatskiy,
659   D., and Wilson, C., J.. 2016. Integrated surface/subsurface permafrost thermal hydrology:
660   model formulation and proof-of-concept simulations Water Resour. Res. 52 6062–77

661   Painter, S. L., and Karra, S.. 2014. Constitutive model for unfrozen water content in subfreezing
662   unsaturated soils *Vadose Zone J.* **13**

663   Peters-Lidard, C. D., Blackburn, E., Liang, X., and Wood, E., F. 1998 The effect of thermal
664   conductivity parameterization on surface energy fluxes and temperatures J. Atmos. 55
665   1209–24

666   Romanovsky, V. E. et al. [The Arctic] Terrestrial Permafrost. In: State of the Climate in 2015.
667   S149-S152 (2015).

668   Rücker, C., Günther, T., and Spitzer, K.: Three-dimensional modelling and inversion of DC
669   resistivity data incorporating topography – I. modelling, Geophys. J. Int., 166, 495–505,
670   https://doi.org/10.1111/j.1365-246X.2006.03010.x, 2006

671   Schuster, P. F., K. M. Schaefer, G. R. Aiken, R. C. Antweiler, J. F. DeWild, J. D. Gryziec, A.
672   Gusmeroli, G. Hugelius, E. Jafarov, D. P. Krabbenhoft, L. Liu, N. Herman-Mercer, C.
673   Mu, D. A. Roth, T. Schaefer, R. G. Striegl, K. P. Wickland, and T. Zhang (2018),
674   Permafrost stores globally significant amount of mercury, Geophys. Res. Lett, 45,
675   GRL56886, https://doi.org/10.1002/2017GL075571

676   Smith, M. and Tice, A.: Measurement of the unfrozen water content of soils comparison of NMR
677   and TDR methods, CRREL Report 88-18, US Army Cold Regions Research and
678   Engineering Lab, 16 pp., 1988.

679   Tran, A. P., Dafflon, B., and Hubbard, S. S.: Coupled land surface–subsurface hy-

680   drogeophysical inverse modeling to estimate soil organic carbon content and explore

681   associated hydrological and thermal dynamics in the Arctic tundra, The Cryosphere, 11,

682   2089-2109, https://doi.org/10.5194/tc-11-2089-2017, 2017.

683   Oleson, K. W., Lawrence, D. M., Gordon, B., Bonan, G. B., Drewniak, B., Huang, M., Koven,

684   C. D., Levis, S., Li, F., Riley, J. W., Subin, Z. M., Swenson, S. C., and Thornton, P. E.:

685   Technical description of version 4.5 of the Community Land Model (CLM), NCAR

686   Technical Note NCAR/TN-503CSTR, 420 pp., https://doi.org/10.5065/D6RR1W7M,

687   2013.

688   Vogel, C.R.. Computational Methods for Inverse Problems. 2002. 183 pages. SIAM. ISBN:

689   9780898715507

690   Yoshikawa, K., Overduin, P., and Harden, J.: Moisture content measurements of moss

691   (Sphagnum spp.) using commercial sensors, Permafrost Periglac., 15, 309–318, 2004.

692   Wang, K., Jafarov, E., Overeem, I., Romanovsky, V., Schaefer, K., Clow, G., Urban, F., Cable,

693   W., Piper, M., Schwalm, C., Zhang, T., Kholodov, A., Sousanes, P., Loso, M., and Hill,

694   K.: A synthesis dataset of permafrost-affected soil thermal conditions for Alaska, USA,

695   Earth Syst. Sci. Data, 10, 2311-2328, https://doi.org/10.5194/essd-10-2311-2018, 2018.